

Exploring thermally induced states in square artificial spin-ice arrays

This content has been downloaded from IOPscience. Please scroll down to see the full text.

2013 New J. Phys. 15 055012

(<http://iopscience.iop.org/1367-2630/15/5/055012>)

View [the table of contents for this issue](#), or go to the [journal homepage](#) for more

Download details:

IP Address: 158.227.184.130

This content was downloaded on 14/11/2013 at 08:49

Please note that [terms and conditions apply](#).

Exploring thermally induced states in square artificial spin-ice arrays

J M Porro^{1,3}, A Bedoya-Pinto¹, A Berger¹ and P Vavassori^{1,2}

¹ CIC nanoGUNE Consolider, Tolosa Hiribidea 76, E-20018 Donostia, Spain

² IKERBASQUE, Basque Foundation for Science, E-48011 Bilbao, Spain

E-mail: tporro@nanogune.eu

New Journal of Physics **15** (2013) 055012 (12pp)

Received 19 December 2012

Published 16 May 2013

Online at <http://www.njp.org/>

doi:10.1088/1367-2630/15/5/055012

Abstract. We present a methodology to explore experimentally the formation of thermally induced long-range ground-state ordering in artificial spin-ice systems. Our novel approach is based on the thermalization from a square artificial spin-ice array of elongated ferromagnetic nanoislands made of a FeNi alloy characterized by a Curie temperature about 100 K lower than that of Permalloy ($\text{Ni}_{81}\text{Fe}_{19}$), which is commonly used for this kind of investigation. The decrease in $M(T)$ when the sample is heated close to its Curie temperature reduces the shape anisotropy barrier of each island and allows us to bring the artificial spin-ice pattern above the blocking temperature of the islands, thus ‘melting’ the spin-ice system, without damaging the sample. The magnetization configuration resulting from the thermal excitation of the islands and the frustrated dipolar interactions among them can be then imaged by magnetic force microscopy or any other kind of magnetic microscopy imaging after cooling down the sample back to room temperature. This thermally induced melting–freezing protocol can be repeated as many times as desired on the same sample and the heating and cooling parameters (max T , heating and cooling rates, number of cycles, application of external fields) varied at will. Thereby, the approach proposed here opens up a pathway to the systematic experimental study of thermally induced frozen states in artificial spin-ice systems, which have been the subject of many recent theoretical studies due to their interesting physical properties but, because of the difficulties in obtaining them in real samples and in a controlled manner, remain experimentally an almost completely unexplored terrain.

³ Author to whom any correspondence should be addressed.



Content from this work may be used under the terms of the [Creative Commons Attribution 3.0 licence](https://creativecommons.org/licenses/by/3.0/).

Any further distribution of this work must maintain attribution to the author(s) and the title of the work, journal citation and DOI.

Many systems found in nature exhibit intrinsic frustration phenomena. For example, frustration occurs between the hydrogen and oxygen atoms in water ice [1], and also appears naturally in rare-earth alloys [2] where magnetic frustration occurs for the magnetic moments of the rare earth ions due to the crystal geometry of the material and they are called, for this reason, ‘spin-ice’ systems. Frustration phenomena occurring spontaneously in natural systems can be studied through the realization of artificial structures mimicking their behavior. Model systems for the case of spin-ice rare-earth alloys are the so-called artificial spin-ice arrays of nanostructures [3, 4], which consist of patterns of interacting ferromagnetic nanoislands showing Ising-like behavior induced by their shape anisotropy. They are organized in different geometrically frustrated arrangements (triangular [5], square [3, 4, 6], hexagonal [7, 8]) with interconnected [7] and isolated [3–5, 8] nanoislands so that the dipole–dipole interactions between neighboring nanomagnets create two-dimensional analogues of real spin-ice systems. Spin-ice systems follow the analogue of the so-called ‘ice rule’ of water ice, where the hydrogen atoms that surround each oxygen atom are arranged in a tetrahedral coordination system, so that two of the hydrogen atoms are close to the central oxygen atom whereas the other two are closer to the surrounding oxygen atoms. In artificial spin-ice systems the magnetic moments of the nanomagnets play the role of the hydrogens and the frustration comes from the geometry of the array and the dipolar interactions that occur in the vertex formed by the edges of the nanomagnets. In this way, at each vertex the magnetic moments of the four nanomagnets will be pointing inwards or outwards, each of them contributing to the net magnetic charge at the vertex center. If we consider a pair of magnetic moments, the energetically favorable configuration is the one in which one points inwards and the other outwards, whereas in the unfavorable one both point inwards or outwards. The case of the square array of nanoislands considered here corresponds to two perpendicular sublattices of lines of interacting nanomagnets so that four edges will converge at each vertex: even in the lowest energy configuration of the magnetization corresponding to the ice rule, viz., two moments pointing inwards and two outwards from the vertex, the two magnetic moments pointing both inwards or outwards are frustrated. All the possible configurations for the magnetic moments at each vertex are shown in figure 1(a), gathered in four groups, each of them with the same magnetostatic energy, net vertex magnetic charge, but different degeneracy. Based on the energies of the four groups of vertex configurations (schematized in figure 1(b)), the lowest energy state of a square artificial spin-ice system involves only Type I vertices. However, the observation of such ground-state ordering in artificial spin-ice systems would depend on the actual process through which the ‘frozen’ state is induced. Most of the studies reported so far rely on direct imaging of the magnetic configurations at room temperature using techniques such as magnetic force microscopy (MFM), x-ray photo emission electron microscopy and Lorentz transmission electron microscopy. Thereby, the magnetic islands ought to be thermally stable, i.e. the system has to be in a frozen state, at room temperature. Choosing the aspect ratio and the volume of the islands large enough so that the energy barrier, mainly due to shape anisotropy, is much higher than thermal excitations at room temperature ensures thermal stability. The artificial spin ice will melt at a temperature corresponding to the blocking temperature T_B of the nanoislands. T_B is the temperature at which the nanoislands undergo a transition from the ferromagnetic to the superparamagnetic regime within a time frame t_m , and it is given in [9] and in a more general way in [10] as:

$$T_B = \frac{KV}{k_B \ln(t_m/t_0)}, \quad (1)$$

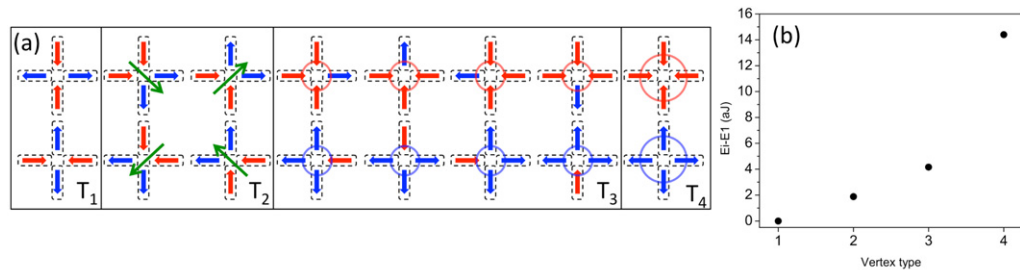


Figure 1. (a) Possible magnetic vertex configurations, gathered in groups with the same energy, ordered from the lowest (T1) to the highest (T4) vertex energy. The T2 vertex carries a net magnetic moment sketched by the arrow in the center; the T3 vertex has a net magnetic charge $q_m = \pm 1$ and the T4 vertex has a net magnetic charge $q_m = \pm 2$. (b) Vertex energy differences ($E_i - E_1$) for each vertex type at room temperature for nanoislands with dimensions $300 \times 100 \times 25$ nm made of Permalloy.

where $K = \frac{1}{2}\mu_0 M_S^2 \Delta N$ is the shape anisotropy constant, V is the volume of the nanoisland, k_B is the Boltzmann constant, t_m is the observation time and t_0 is the attempt time of the order of 10^{-10} s. ΔN is the difference between the demagnetizing factors along the in-plane short and long axes of the island. Above this temperature, the nanoislands retain their magnetic moments, provided $T_B < T_C$, but thermal energy makes them flip continuously between the two stable directions dictated by the shape anisotropy. However, for nanoislands of a size that can be fabricated using state-of-the-art lithography with sufficient control of the island geometry, thermal ‘melting’ of the system would require such a high temperature that it would damage the sample, eventually destroying it. For $300 \times 100 \times 25$ nm³ islands, such as those investigated here, and assuming $t_m = 1$ s and that the material of the nanoislands is Py (saturation magnetization at 0 K $M_S = 860 \times 10^3$ A m⁻¹), we obtain $T_B \approx 10^5$ K.

In reality, due to the $M_S(T)$ dependence, the nanoislands will reach their T_B at a lower T close to T_C , which is however still high enough to damage permanently a sample made of standard ferromagnetic materials such as Fe, Co or Py as those used so far. For example, considering the $M_S(T)$ dependence of Py ($T_C = 853$ K) we obtain $T_B = 847$ K for islands having the same size and shape as above. Initial attempts at achieving the thermal melting of artificial spin-ice arrays with islands made of Py showed that such a T_B will make the sample unusable after the annealing. Therefore, attempts to induce ground-state ordering have been carried out by applying external magnetic fields. In detail, Wang *et al* [11] proposed a demagnetizing protocol consisting of applying ac external magnetic fields of decreasing amplitude, from saturation value to zero, while the sample is rotated about the surface normal at a high speed of 1000 rotations per minute (rpm). The final magnetic states obtained in this way show only a short-range ground-state ordering, with a small percentage of vertices in the highest energy Type IV configuration. A field-induced demagnetizing protocol that can induce long-range ground-state ordering has yet to be found.

Recently, studies conducted on as-grown samples proved that ground-state ordering over wide regions of the array can be achieved [4]. The explanation of such observations relies on the fact that when the nanoislands are being grown, during the initial stage of the deposition of the magnetic material, the thickness, and thus the volume, of the nanoislands is small enough

so that the shape anisotropy energy E_A ,

$$E_A = KV = \frac{1}{2}\mu_0 M_S^2 \Delta N V, \quad (2)$$

i.e. the energy barrier that has to be overcome in order to flip the magnetic moment of the nanoisland, is comparable with the thermal energy E_{th} ,

$$E_{th} = k_B T, \quad (3)$$

at the deposition temperature. At the same time, the dipolar interactions between neighboring nanoislands are not negligible so that their magnetic moments' orientations at each vertex of the array can try to arrange themselves in the most favorable configuration before the magnetic moments of the nanoislands become frozen. This gradually happens as the thickness of the nanoislands increases during the growth producing the increase of the anisotropy energy barrier above the thermal energy excitations. The results reported on these measurements show long-range ground-state (Type I vertices) ordering regions in the arrays investigated separated by narrow boundaries made of Type II and Type III vertices identified as elementary excitations of the systems [4].

These findings demonstrated that thermal fluctuations can indeed induce long-range ground-state ordering in artificial spin-ice systems and, subsequently, they triggered intense theoretical and modeling efforts. These studies in fact predict novel and intriguing physical properties related to the presence of long-range ground-state ordering domains and their boundaries [12, 13]. For example, these studies show links to the physics of the formation and propagation of magnetic monopole excitations and Dirac strings [4, 14, 15].

However, the study of the as-grown magnetization state is a limited methodology to investigate the ground-state ordering formation since it is a single-shot approach, which prevents any systematic study of the physical processes. In addition, if any external perturbation destroys the as-grown state it cannot be recovered.

Devising an alternative method that removes these limitations would open up a new pathway for the systematic study of the interesting physics of artificial spin ice characterized by long-range ground-state ordered configurations. From what was discussed above, it is apparent that heating the sample above T_B would require the fabrication of very small nanoislands in order to reduce T_B to values that can be reached without damaging the sample.

As an example, given the room temperature magnetization of Permalloy and considering a T_B of 750 K as a reasonable value of temperature that can be reached without causing permanent damage to the sample, a thickness of 1 nm, and setting the aspect ratio of the nanoisland to 2, we obtain using the equation given above for T_B that the nanoisland should have lateral dimensions of $20 \times 10 \text{ nm}^2$. The fabrication of such small nanostructures with the required uniformity over large arrays is a tremendous challenge, beyond the reach of current state-of-the-art lithography [16].⁴

To circumvent this problem we pursued a different pathway. We kept the dimensions of the nanoislands in a regime where we can control the lithography process at the level required to obtain high-quality nanostructures, so that the distributions in size, shape and defects are not an issue for determining their magnetic properties and thermal relaxation. We instead changed

⁴ A recent paper appeared in *Nature Physics* reports on thermally induced magnetic relaxation in an artificial Kagome spin-ice system made of Py nanoislands with dimensions $470 \times 170 \times 3 \text{ nm}$ at temperatures near room temperature. The justification given in that paper for such a behavior, which is apparently in contrast with what we are stating here, was that the magnetization saturation of the very thin Py layer forming the nanoislands is about 10 times lower than the bulk value assumed in our calculations.

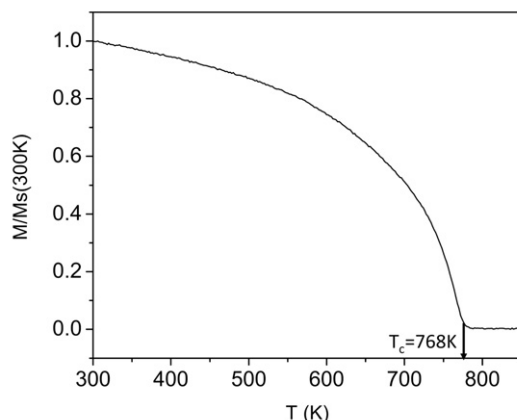


Figure 2. Magnetization versus temperature curve of a 25 nm thick film of the $\text{Ni}_{87}\text{Fe}_{13}$ alloy normalized to the room temperature magnetization value, measured with a vibrating sample magnetometer. The Curie temperature of the alloy is marked in the graph.

the magnetic material composition in order to reduce T_C to the extent that we can reach a temperature regime above T_B without destroying the nanostructures. The T_C of Py is 853 K, which is too high for the purpose since as we have discussed above T_B will be close to T_C . We therefore deposited nickel–iron alloys where we slightly varied the Ni and Fe content since T_C in these alloys is known to depend on the composition [17]. By depositing a nickel–iron alloy with 87% Ni and 13% Fe, we achieved a $T_C = 768$ K, as measured with a vibrating sample magnetometer equipped with an oven, which corresponds to a reduction of T_C of approximately 100 K with respect to standard Py. The measured M_S versus T curve of a 25 nm thick film made of this $\text{Ni}_{87}\text{Fe}_{13}$ alloy is shown in figure 2. This alloy was then used to fabricate arrays of nanoislands 300 nm long, 100 nm wide and 25 nm thick forming an artificial spin-ice pattern nanostructure with a lattice parameter of 400 nm by means of electron beam lithography. These nanoislands have an Ising-like bistable magnetization behavior, a mandatory requirement for nanostructures forming artificial spin-ice patterns. The magnetic alloy was deposited at a rate of 0.8 \AA s^{-1} onto the electron-beam lithography structured sample using an electron-beam evaporator, while rotating the sample at 15 rpm to obtain a homogeneous distribution of the magnetic material. Figure 3 shows a scanning electron microscopy image of one region of the sample, together with a zoomed-out image of the same sample to observe the homogeneity and high quality of the array.

In figure 3 also, the 16 different possible vertex configurations, as they appear in different MFM images taken during the realization of the experiments, are shown as a guide to the eye for the interpretation of the MFM images that will be discussed later. The magnetization of the $\text{Ni}_{87}\text{Fe}_{13}$ alloy at room temperature is $686 \times 10^3 \text{ A m}^{-1}$, i.e. lower than that of Py ($775 \times 10^3 \text{ A m}^{-1}$), but this is not a relevant issue by itself since the energy barrier at room temperature is still 10^4 times bigger than the thermal energy excitations.

The blocking temperature of the nanoislands can be evaluated as follows from the expression of T_B given above that can be cast in the following form:

$$\ln\left(\frac{1}{t_0}\right) k_B T_B = \frac{1}{2} \mu_0 M_S^2(T_B) \Delta N V, \quad (4)$$

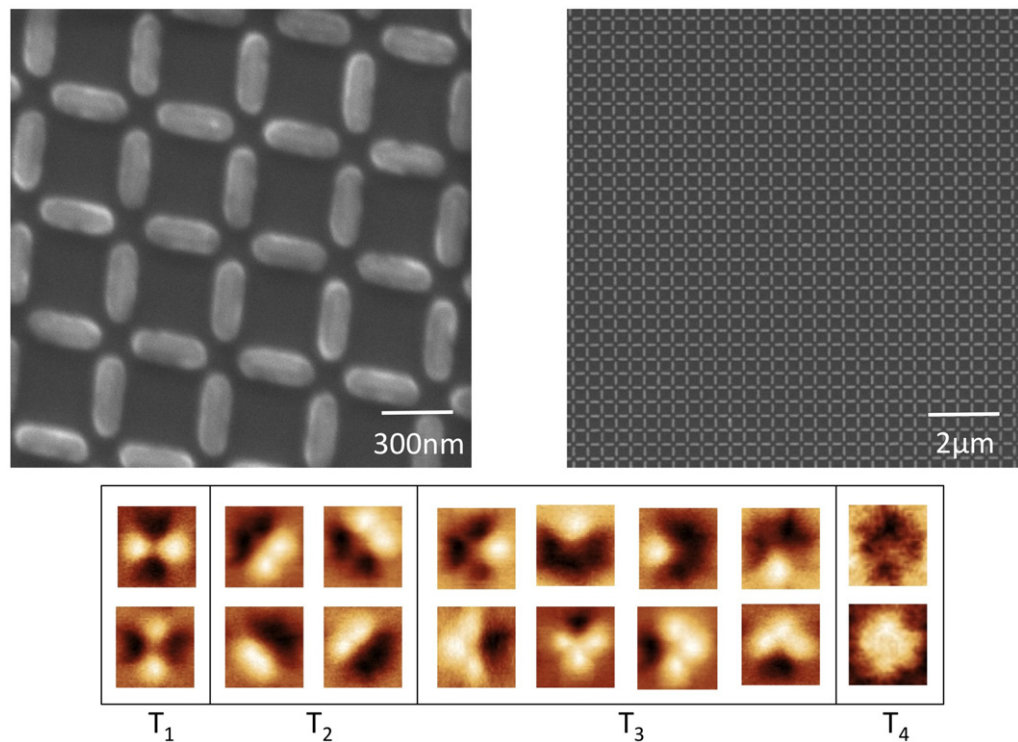


Figure 3. SEM images of the nanofabricated artificial spin-ice pattern (up) and MFM images of each of the 16 possible vertex configurations imaged during the realization of the experiments (down).

where we specifically use in the expression of the shape anisotropy the temperature dependence of M_S , taken from the experimental curve shown in figure 2, and we used $t_m = 1$ s considering that the typical heating and cooling rates used in our experiments are about 1 K s^{-1} . The other parameters are $\Delta N = 0.146$ (calculated using the expressions given in [18]) and $V \approx 7.5 \times 10^{-22} \text{ m}^3$ is the volume of a nanoisland. This equation is solved graphically in figure 4, which shows that the intersection between the thermal energy activation term (the first term in equation (4)) and the shape anisotropy energy (the second term in equation (4)) occurs at $T_B = 765 \text{ K}$. At this T_B , the saturation magnetization has a value of $M_S(T = 765 \text{ K}) = 90.5 \times 10^3 \text{ A m}^{-1}$, which we then used to evaluate the dipolar magnetostatic energies at $T = 765 \text{ K}$ of each of the four degenerate groups of vertex types, namely Types I–IV, sketched in figure 1. Each energy was computed using the OOMMF micromagnetics simulation platform⁵, for which we used a simulation unit comprising four nanoislands forming a vertex with the value of M_S specified above and with the orientation of M set according to each vertex type. For the simulation we used a cell size of 5 nm side, which is lower than the exchange length of Py (5.4 nm) used as a reference also for our alloy. The four total magnetostatic energies (demagnetizing energy plus magnetostatic dipolar interaction energy) obtained are 0.79 , 0.852 , 0.91 and 1.127 aJ on going from the Type I to Type IV vertex, and their differences with the Type I vertex energy are plotted in figure 4. If we bring the system above T_C , the remagnetizing process during the cooling down across T_B should occur as follows. Initially, just below T_C , the four vertex-type configurations would be equally populated since $M_S \approx 0$ and therefore the

⁵ OOMMF code made by NIST <http://math.nist.gov/ommf/>.

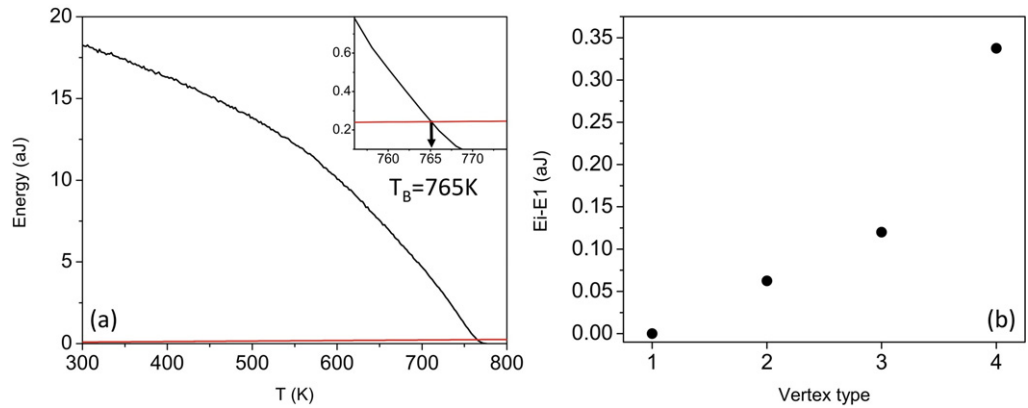


Figure 4. (a) Shape anisotropy energy (black) and thermal energy $k_B T$ (red) as a function of temperature, with the inset showing the critical temperature zone, with the blocking temperature of the nanoislands made of $\text{Ni}_{87}\text{Fe}_{13}$ alloy marked. (b) Vertex energy differences ($E_i - E_1$) as a function of the vertex type at $T_B = 765$ K.

dipolar interactions among the islands are negligible, viz. all 16 vertex-type configurations are degenerate. As we reduce T approaching T_B , M_S increases and so does the dipolar interaction, gradually removing the degeneracy of the four vertex configurations. We therefore should expect a progressive depopulation of the high-energy states as the thermal energy will favor unidirectional jumps overcoming the shape anisotropy barrier in one direction, from an energy state to one with lower energy. The reverse process will become more and more unlikely as in order to jump from a less energetic vertex state to the next higher energetic one the activation energy is higher than that due to the shape anisotropy barrier (the only one to overcome in the downward channel), because of the additional positive energy difference between the two vertex-type configurations. Eventually, as T_B is being approached, the energy difference between the states becomes so large that the upward channel freezes before all thermal jumps become impossible (i.e. below T_B). To realize this we can consider in detail the energies plotted in figure 4. At T_B , the energy difference between Type II and Type I vertices is around 0.063 aJ, which corresponds to 390 meV. The energy difference between Type III and Type I vertices is 750 meV, and between Type IV and Type I vertices 2.113 eV. These energy differences compare with a Boltzmann term $k_B T$ of only 66 meV at T_B . Based on these assumptions, when cooling down the sample from above T_C , below T_B we should expect to end up with only Type I vertices frozen in the sample, which corresponds to the ground state of the artificial spin-ice system.

We therefore repeatedly annealed our sample to around 800 K, above both T_C and T_B , and cooled it down to room temperature at a cooling rate of 1 K s^{-1} . The resulting magnetization states after the annealing processes were investigated by means of MFM. Two $15 \times 15 \mu\text{m}^2$ MFM images of the frozen-in demagnetized states are shown in figure 5. As can be seen from figures 5(a) and (b), the room temperature magnetization distribution shows a long-range ground-state ordering of the artificial spin-ice magnetic moments, comparable with the ones obtained in the as-grown state and studied by Morgan *et al* in [4]. To better appreciate the similarity of the resulting configurations, in the lower panels of figures 5(a) and (b) we display the MFM images in the corresponding upper panels using the same contrast color scheme used in [4] and compare the image with that obtained in that work, which is shown in figure 5(c). The lower panel of figure 5(c) shows a zoomed-in region of the as-grown state observed in [4] over

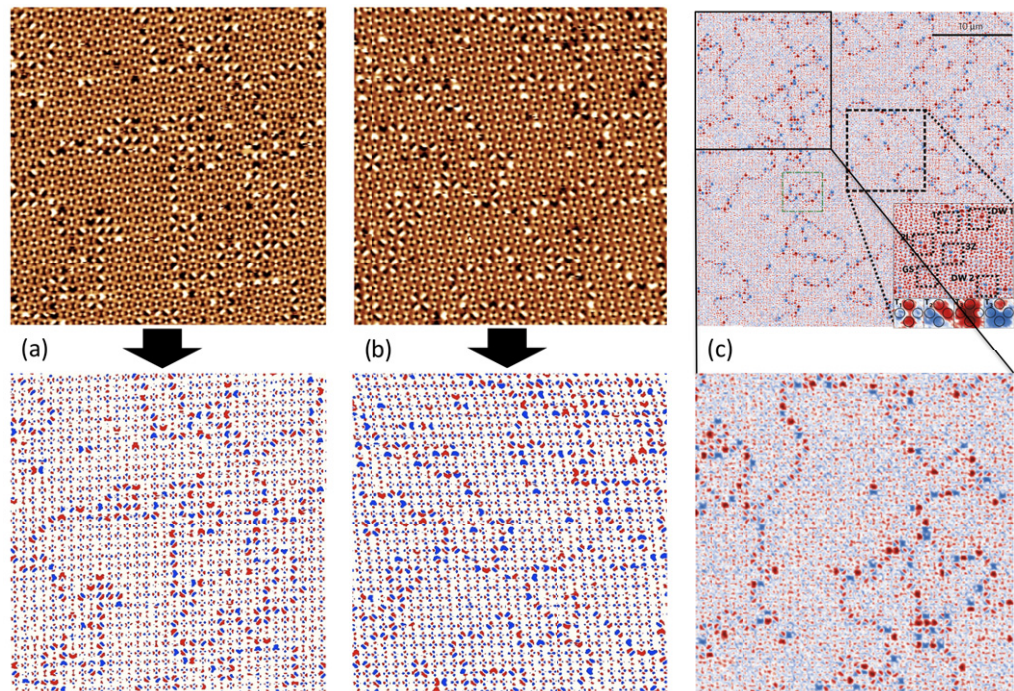


Figure 5. $15 \times 15 \mu\text{m}^2$ MFM images of two regions of the square artificial spin-ice pattern after applying thermal annealing demagnetization protocols heating the pattern above its blocking temperature ((a) and (b)), showing long-range ground-state square-ice regions separated by Type II and Type III vertex chains. The lower panels correspond to the MFM images shown above them with the color code used in [4], to compare them with the as-grown magnetization state obtained in [4], which is observed in (c). A zoomed-in $15 \times 15 \mu\text{m}^2$ MFM image region is shown in the lower panel of (c) for a side-to-side comparison with the ones observed in (a) and (b) after applying the thermal annealing demagnetization protocol. Panel (c) has been reprinted and adapted by permission from Macmillan Publishers Ltd: Morgan *et al Nature Phys.* 7 75, copyright 2011.

an area with a similar size as that shown in figures 5(a) and (b), for side-to-side comparison purposes. A visual comparison between figures 5(a) and (c) shows some differences in the domain boundaries between the ground-state regions. Nevertheless, if we image a different region of the sample, as shown in figure 5(b), these domain boundaries are more similar to those displayed in figure 5(c). Similar variations of the domain boundary structure were also reported by Morgan *et al* in the supplementary information given in [4], and can be most likely due to a random distribution of the islands' imperfections. This thermal demagnetizing protocol was applied several times, and the resulting magnetization states were analyzed via MFM, showing always similar results on the obtained room temperature magnetization state. We conducted a statistical analysis of the vertex-type population observed after each thermal annealing and found that $74.3 \pm 4.2\%$ of the vertices were of Type I, $20.1 \pm 2.0\%$ were of Type II and only $5.6 \pm 2.1\%$ were of Type III. We did not observe a single vertex in a Type IV configuration, while some of them can be found in the as-grown state presented by

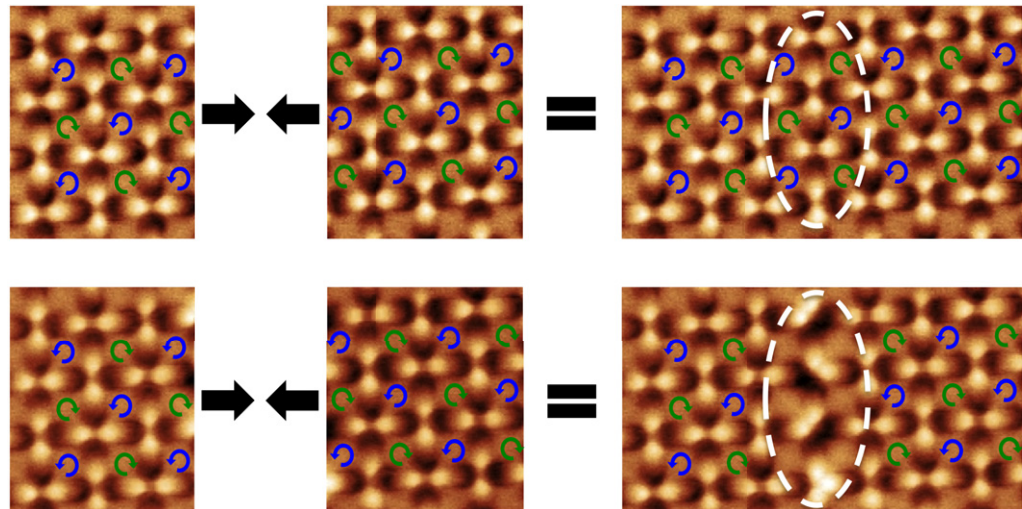


Figure 6. Formation of large ground-state regions on the thermal demagnetization protocol when two opposite chirality Type I vertex regions merge (up), and formation of a ‘domain wall’ region (marked with a white dashed line) with Type II and Type III vertices when two Type I vertex regions with the same chirality merge (down).

Morgan *et al* in [4], which is a remarkable difference between our approach and the one presented in [4]. As discussed previously, in a perfect sample this annealing process should, in principle, lead to the formation of a magnetization state with only Type I vertices, i.e. the ground state of our artificial spin-ice pattern. A possible explanation for this discrepancy can be traced to the unavoidable defects, such as size and shape distribution, due to the nanofabrication process, so that not all the nanoislands are identical, which means that there will be a distribution of blocking temperatures T_B [19]. During the cooling, the distribution of T_B would lead to the nucleation and freezing of ground-state ordered regions in different portions of the sample, those with higher T_B . These initially frozen regions will be a seed of ground-state order at their boundary, causing their progressive expansion as T decreases further. It can be noted by inspection of the MFM image in figure 5(a) (or (b)) that in the areas of ground-state ordering, Type I vertices alternate with opposite chirality along horizontal and vertical lines, as sketched in figure 6. When two (or more) of these regions come together, they can merge forming a unique broader region if the chirality of the vertices at their border matches or, in case there is no matching, a boundary of Type II and/or Type III vertices is formed, as schematically shown in the lower panel of figure 6. This process shares many similarities with the remagnetization of a sample via magnetic domain formation and expansion.

The final result would be a series of ‘domains’ of Type I vertices separated by ‘domain walls’ made predominantly by Type II vertices with some ‘defects’ of Type III, as we indeed recurrently observed in our MFM images. The quite broad domain size distribution observed in the MFM images could be due to the fact that the freezing temperature window is very narrow, so that during the cooling we might not give the system enough time to fluctuate out the smaller domains.

It is interesting to compare the frozen states achieved via our thermal demagnetizing protocol with those obtained via the external ac field-induced demagnetizing protocol often

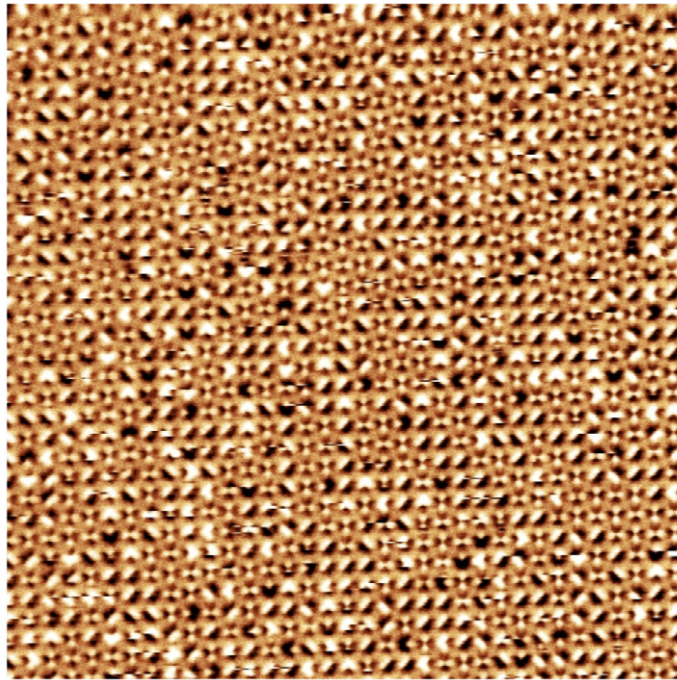


Figure 7. $15 \times 15 \mu\text{m}^2$ MFM image of the square artificial spin-ice pattern after applying an in-plane ac magnetic field rotating demagnetization protocol, showing short-range ground-state square-ice regions.

used in the literature and originally proposed by Wang *et al* [11]. Following [11], the protocol consists of applying an in-plane magnetic field starting from above the saturation of the nanoislands and reducing it toward zero, stepping the field strength down while flipping the field direction in every step. At the same time the sample is rotated at 1000 rpm. We started the demagnetizing protocol by applying an in-plane magnetic field of 1300 Oe, reducing it to 816 Oe in steps of 32.6 Oe, followed by steps of 16.3 Oe until we reach zero applied field, flipping the magnetization direction in each step, and with a step duration of 1 s, while the sample was rotating at a speed of 1000 rpm. We applied this demagnetization protocol at different times, observing always similar results to those obtained by Wang *et al*. An MFM image over an area of $15 \times 15 \mu\text{m}^2$ of one of the remanent magnetization states achieved in the artificial spin-ice pattern is shown in figure 7. One can immediately appreciate that the state achieved is qualitatively different from those obtained via the thermal demagnetization since only short-range ground-state ordering is now observed with the presence of a few high-energy Type IV vertices. We conducted a statistical analysis of the vertex types population: $48.1 \pm 3.7\%$ of the vertices were of Type I, $41.3 \pm 2.7\%$ of Type II, $9.2 \pm 0.8\%$ of Type III and $1.4 \pm 0.3\%$ of Type IV.

The two results of the statistical analysis are displayed together in figure 8 for a side-to-side comparison. By combining these results with those obtained for the thermal demagnetization, we observe that in the case of the thermal process the overall energy of the system is substantially lower than that obtained via the ac field demagnetization.

Following the methodology presented here, a wide landscape of possible experiments has opened up. As an example, it is now possible to provide a solid experimental base for theoretical

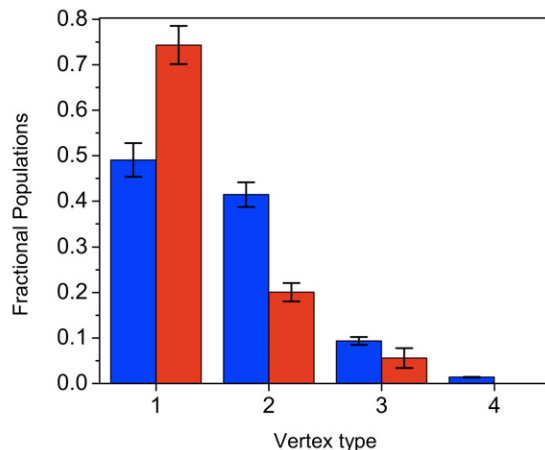


Figure 8. Bar plot showing the vertex populations for each demagnetization protocol. The in-plane ac magnetic field rotating demagnetization protocol vertex populations are shown in blue, and the thermal annealing demagnetization protocol vertex populations are shown in red.

studies performed on the thermalization of artificial spin-ice patterns [12]. By varying the cooling rate or by performing several minor temperature loops, changing for instance the maximum temperature reached at each loop, one can investigate the formation and the structure of the Type II and Type III ‘domain wall’ boundaries between ground-state ordering domains as well as domain size distribution versus cooling rate. Another possible experiment to be performed with our thermal demagnetization protocol is the study of how defects and vacancies of individual nanoislands in an artificial spin-ice pattern lead to the formation of the ground-state ordering, as an experimental verification of what is presented in [19]. Since our approach works independently of the island volume, one can also study how the variation of the thickness of the nanoislands, namely the strength of the dipolar interaction, affects the final ground-state ordering obtained after applying the thermal demagnetization protocol. A quick estimate of $(M_S(T_B)t)^2$ as a function of the thickness indicates that the dipolar interaction strength increases as we increase the thickness. It is worth mentioning, in conclusion, that the approach described is general and not limited to the actual material employed here, viz. $\text{Ni}_{87}\text{Fe}_{13}$, but it can be implemented using other materials. For instance, pure Ni has a T_C of 673 K, about 100 K lower than our alloy. The utilization of Ni, or in general any other ferromagnetic material with a sufficiently low T_C , would allow an implementation of our approach. For specific materials, it could even allow performing the thermal demagnetization while directly observing the sample with the MFM.

Acknowledgments

We acknowledge funding from the Basque Government under program no. PI2012-47 and the Spanish MICINN under project no. MAT2012-36844. JMP acknowledges funding from the Basque Government fellowship no. BFI09.289. PV acknowledges funding from IKERBASQUE, the Basque Science Foundation.

References

- [1] Bramwell S T and Gingras M J P 2001 *Science* **294** 1495
- [2] Harris M J, Bramwell S T, McMorrow D F, Zeiske T and Godfrey K W 1997 *Phys. Rev. Lett.* **79** 2554
- [3] Wang R F *et al* 2006 *Nature* **439** 303
- [4] Morgan J P, Stein A, Langridge S and Marrows C H 2011 *Nature Phys.* **7** 75
- [5] Mól L A S, Pereira A R and Moura-Melo W A 2012 *Phys. Rev. B* **85** 184410
- [6] Remhof A, Schumann A, Westphalen A and Zabel H 2008 *Phys. Rev. B* **77** 134409
- [7] Ladak S, Read D E, Perkins G K, Cohen L F and Branford W R 2010 *Nature Phys.* **6** 359–363
- [8] Mengotti E, Heyderman L J, Fraile Rodriguez A, Nolting F, Hügli R V and Braun H B 2011 *Nature Phys.* **7** 68–74
- [9] Néel L 1949 *Ann. Géophys.* **5** 99–136
- [10] Braun H-B 2012 *Adv. Phys.* **61** 1
- [11] Wang R F *et al* 2007 *J. Appl. Phys.* **101** 09J104
- [12] Burkidis Z, Livesey K L, Morgan J P, Akerman J, Stein A, Langridge S, Marrows C H and Stamps R L 2012 *New J. Phys.* **14** 035014
- [13] Greaves S J and Muraoka H 2012 *J. Appl. Phys.* **112** 043909
- [14] Ladak S, Walton S K, Zeissler K, Tyliczszak T, Read D E, Branford W R and Cohen L F 2012 *New J. Phys.* **14** 045010
- [15] Nascimento F S, Mól L A S, Moura-Melo W A and Pereira A R 2012 *New J. Phys.* **14** 115019
- [16] Farhan A, Derlet P M, Kleibert A, Balan A, Chopdekar R V, Wyss M, Anghinolfi L, Nolting F and Heyderman L J 2013 *Nat. Phys.* doi:[10.1038/nphys2613](https://doi.org/10.1038/nphys2613)
- [17] Miller K J, Sofman M, McNerny K and McHenry M E 2010 *J. Appl. Phys.* **107** 09A305
- [18] Osborn J A 1945 *Phys. Rev.* **67** 351–7
- [19] Silva R C, Lopes R J C, Mól L A S, Moura-Melo W A, Wysin G M and Pereira R 2013 *Phys. Rev. B* **87** 014414